

FOMALHAUT'S DEBRIS DISK AND PLANET: MEASURING THE MASS AND ORBIT OF FOMALHAUT B USING DISK MORPHOLOGY

E. CHIANG^{1,2}, E. KITE², P. KALAS¹, J. R. GRAHAM¹, & M. CLAMPIN³

Submitted to *ApJ* 09/30/08; Accepted 11/07/08

ABSTRACT

Following the discovery of the exoplanet candidate Fomalhaut b (Fom b), we present a numerical model of how Fomalhaut's debris disk is gravitationally shaped by an interior planet. To produce the observed disk morphology, Fom b must have a mass $M_{\text{pl}} < 3M_{\text{J}}$, an orbital semimajor axis $a_{\text{pl}} > 101.5$ AU, and an orbital eccentricity $e_{\text{pl}} = 0.11\text{--}0.13$. These conclusions are independent of Fom b's photometry and support the case that Fom b is a planet. To not disrupt the disk, more massive planets must have smaller orbits farther removed from the disk; thus, future astrometric measurement of Fom b's orbit, combined with our model of planet-disk interaction, can be used to determine the mass more precisely. If $a_{\text{pl}} \approx 114$ AU, as suggested by a preliminary and model-dependent analysis of Fom b's astrometry, then our dynamical model implies $M_{\text{pl}} \approx 0.4M_{\text{J}}$. The inner edge of the debris disk at $a \approx 133$ AU lies at the periphery of Fom b's chaotic zone, and the mean disk eccentricity of $e \approx 0.11$ is secularly forced by the planet, supporting predictions made prior to the discovery of Fom b. However, previous mass constraints based on disk morphology rely on several oversimplifications. We explain why our new constraint of $M_{\text{pl}} < 3M_{\text{J}}$ is more reliable. It is based on a global model of the disk that is not restricted to the chaotic zone boundary. Moreover, we screen disk parent bodies for dynamical stability over the system age of ~ 100 Myr, and model them separately from their dust grain progeny; the latter's orbits are strongly affected by radiation pressure and their lifetimes are limited to ~ 0.1 Myr by destructive grain-grain collisions. Parent bodies are evacuated from mean-motion resonances with Fom b; these empty resonances are akin to the Kirkwood gaps opened by Jupiter. The belt contains at least $3M_{\oplus}$ of solids that are grinding down to dust, their velocity dispersions stirred so strongly by Fom b that collisions are destructive. Such a large mass in solids is consistent with Fom b having formed *in situ*.

Subject headings: stars: planetary systems — stars: circumstellar matter — planetary systems: protoplanetary disks — celestial mechanics — stars: individual (Fomalhaut)

1. INTRODUCTION

A common proper motion companion to Fomalhaut has been imaged by Kalas et al. (2008, hereafter K08) using the Hubble Space Telescope Advanced Camera for Surveys (HST ACS) coronagraph. Fomalhaut b (Fom b) orbits interior to the system's well-known circumstellar belt of dust (e.g., Holland et al. 1998; Kalas et al. 2005, hereafter K05, and references therein). With observations at only two epochs to date, the orbit of Fom b is uncertain, but a semimajor axis of approximately 115 AU is consistent with the data. While Fom b's ultra-low luminosity leaves little doubt that it is of remarkably low mass, sitting well below the regime of brown dwarfs, the question remains just how low its mass is.

Based on the observed broadband spectrum of Fom b, K08 estimate an upper limit on the mass M_{pl} of about $3M_{\text{J}}$. We recapitulate their reasoning as follows. Fom b is detected in HST's F814W (0.7–0.9 μm) and F606W (0.45–0.7 μm) passbands in 2006. The F606W flux is variable; the flux in 2006 was about half that in 2004. Observations in 2005 with Keck in H band (1.5–1.8 μm) and in 2008 with Gemini in L-prime (3.2–4 μm) give only

upper limits.

The F814W flux (observed only in 2006; imaging was not attempted in 2004 for this passband) can be reproduced by thermal emission from a 2–4 M_{J} , 200-Myr-old planet that formed by core accretion and is of supersolar metallicity (Hubickyj et al. 2005; Fortney et al. 2008). Unfortunately, this same model atmosphere underpredicts, by more than an order of magnitude, the F606W fluxes. At the same time it overpredicts the H-band 3σ upper limit by a factor of a few, and is marginally consistent with the L-prime 3σ upper limit. From considerations outlined by K08, we can construct two, not entirely exclusive hypotheses. Hypothesis one: F814W still traces planetary thermal emission, F606W is contaminated by variable H α emission, and the atmospheric model requires revision in H band. The H α hypothesis is inspired by variable H α emission from chromospherically active and/or accreting low-mass stars and brown dwarfs. The puzzling brown dwarf GQ Lup B offers a possible precedent (Marois et al. 2007); in either the case of Fom b or that of GQ Lup B, the H α luminosity necessary to explain the anomalously large F606W flux is $\sim 1\%$ that of the bolometric luminosity (unfortunately in neither case has an optical spectrum been taken). As for uncertainties in model exoplanet atmospheres (Fortney et al. 2008; Burrows et al. 2003), these appear greater in H band than in F814W; the various models disagree with each other at near-infrared wavelengths by factors

¹ Department of Astronomy, 601 Campbell Hall, University of California at Berkeley, Berkeley, CA 94720, USA

² Department of Earth and Planetary Sciences, 307 McCone Hall, University of California at Berkeley, Berkeley, CA 94720, USA

³ Goddard Space Flight Center, Greenbelt, MD 20771, USA
Electronic address: echiang@astro.berkeley.edu

of a few. Hypothesis two: both F814W and F606W are contaminated by starlight reflected off an optically thick circumplanetary disk, and the F606W variability arises from variable disk accretion onto the planet, possibly implicating $H\alpha$ again. To explain the detected fluxes in 2006 using reflected light alone, such a disk would have to be comparable in size to the orbits of Jupiter’s Galilean satellites. It is not clear, however, how such a disk would survive for the system age of ~ 100 Myr; protosatellite disks are thought to evolve on timescales shorter than a few Myr (e.g., Canup & Ward 2002; Mosqueira & Estrada 2003).

Since both hypotheses admit the possibility of additional sources of luminosity apart from planetary thermal emission, the $3M_J$ inferred from the observed F814W flux should be considered an upper limit. As a whole, this interpretation of Fom b’s photometry is preliminary, subject to significant revision as both observations and theory improve.

An alternative route to probing the properties of Fom b is to exploit the morphology of the circumstellar belt. Prior to the discovery of Fom b, this approach was taken by Quillen (2006, hereafter Q06), who built on earlier work by Wyatt et al. (1999). The striking intrinsic ellipticity of the belt of $e \approx 0.11$ can be forced by secular gravitational interaction with a planet on a similarly eccentric orbit interior to the belt.⁴ Fomalhaut b was predicted by Q06 to occupy an orbit of eccentricity 0.1 and semimajor axis ~ 119 AU, and to have a mass between about 2×10^{-5} and 7×10^{-5} that of the central star. For a stellar mass of $M_* = 2.3M_\odot$, this range corresponds to ~ 0.05 – $0.2 M_J$.

The predictions of Q06 rest on the idea that the belt inner edge, at semimajor axis $a_{\text{inner}} = 133$ AU, is located at the outer boundary of Fom b’s chaotic zone. The chaotic zone is a swath of space enclosing the planet’s orbit inside of which test particle orbits are chaotic and short-lived, as a consequence of overlapping first-order mean-motion resonances (Wisdom 1980). The semimajor axis a_{chaotic} at the edge of this chaotic zone is displaced to either side of the planet’s semimajor axis a_{pl} by

$$\Delta a_{\text{chaotic}} = |a_{\text{chaotic}} - a_{\text{pl}}| \approx 1.3 \mu^{2/7} \quad (1)$$

where $\mu = M_{\text{pl}}/M_*$. The coefficient of 1.3 arises from Wisdom’s approximate scaling theory. Though (1) is derived for the case of a planet that occupies a circular orbit and that interacts with test particles on nearly circular orbits, Quillen & Faber (2006) find that the $\mu^{2/7}$ scaling law holds also for a planet on a moderately eccentric orbit, interacting with particles on secularly forced eccentric orbits. Quillen & Faber (2006) prefer, however, the coefficient of 1.5 that originates from the numerical integrations and eccentricity growth criterion of Duncan et al. (1989).⁵ Our work supports the assignment $a_{\text{inner}} = a_{\text{chaotic}}$ made by Q06. However, we will

⁴ See the textbook by Murray & Dermott (2000) for an introduction to secular perturbation theory, which essentially treats masses as orbit-averaged elliptical wires.

⁵ Duncan et al. (1989) also provide a simple explanation of behavior within the chaotic zone (for the case of circular orbits): particles residing there are perturbed so strongly by the planet at each conjunction that successive conjunctions occur at uncorrelated longitudes; consequently the particle undergoes a random walk in semimajor axis and eccentricity, with steps in the walk corresponding to impulses at every conjunction.

calculate still a third coefficient that best reproduces the HST images of Fomalhaut’s belt; see our equation (16).

The discovery of Fom b orbiting just interior to the dust belt appears to confirm the expectation of K05, made quantitative by Q06, that a planet is responsible for truncating the inner edge of the belt. There are, however, several reasons to question the published dynamical mass constraint of $0.05 \lesssim M_{\text{pl}}(M_J) \lesssim 0.2$, based as it is on belt morphology:

1. Belt properties depend weakly on planet mass. For example, $\Delta a_{\text{chaotic}}$, which governs the relative locations of the belt inner edge and the planet, scales only as $M_{\text{pl}}^{2/7}$. Similarly weak powers describe how the velocity dispersion at the boundary of the chaotic zone depends on M_{pl} ; Q06 parlay this dependence into an upper limit on M_{pl} , on the grounds that too large a velocity dispersion violates the observed sharpness of the belt’s inner edge. (We will see in our work that this argument does not fully capture the actual behavior because it neglects how belt particles located some distance from the chaotic zone boundary influence the observed sharpness of the edge. In other words, sharpness can only be reliably computed with a global model, not one that examines the chaotic zone boundary only. See Figure 8 and the related discussion in §3.3.1.)
2. The published dynamical upper mass limit is based on the purely gravitational, collisionless behavior of test particles. But the HST observations of Fomalhaut’s belt are of dust grains, which are influenced by stellar radiation pressure and interparticle collisions. As explained in §2 (see also Strubbe & Chiang 2006), the scattered light observations are likely dominated by the smallest grains still bound to the star. Of all the solid material orbiting Fomalhaut, such grains have the largest ratios of surface area to mass and are the most seriously affected by radiative forces and collisions.
3. The lower dynamical mass limit is also suspect because it is premised on particles colliding indestructibly and diffusing as members of a viscous circular ring. The argument underlying the lower limit is that the planet mass cannot be too small lest dust grains diffuse into the chaotic zone by interparticle collisions, before the planet can gravitationally eject them (see also Quillen 2007). But dust particles, colliding at minimum speeds of ~ 100 m/s (see our §2), likely shatter one another. Moreover, their trajectories are highly elliptical as a consequence of radiation pressure (Strubbe & Chiang 2006). Their dynamics seem poorly described by a diffusion equation that conserves particle number, has constant diffusivity, and assumes circular orbits.

In this work we present a new numerical model of the Fomalhaut dust belt. It accounts not only for gravitational sculpting by Fom b, but also for the finite collisional lifetime of dust, the size distribution of grains, and radiation forces (including Poynting-Robertson drag,

though it is of minor importance compared to other perturbations). Though we do not go as far as generating a model scattered light image to compare with observations, we take the first step towards this goal by calculating the detailed shape of the belt’s vertical optical depth, τ_{\perp} , as a function of semimajor axis a . We compare this optical depth profile with the corresponding profile of the K05 scattered light model, which in turn was fitted directly to the HST images. From this comparison we constrain the mass and orbit of Fom b: we calculate the possible combinations of planet mass M_{pl} , orbital semimajor axis a_{pl} , and orbital eccentricity e_{pl} . These results are independent of any measurement of Fom b, in particular of its spectrum. Only as a final extra step do we use information on Fom b’s observed stellocentric distance to see if some of our mass-orbit combinations might be ruled out.

Our work corroborates the overall picture of Q06—that the planet’s chaotic zone truncates the inner edge of the belt, and that the planet’s orbital eccentricity induces a similar mean eccentricity in the belt (Wyatt et al. 1999)—but we introduce enough improvements, especially with regards to our separate handling of unobservable parent bodies and observable dust grains, that our dynamical constraint on Fom b’s mass supersedes that of Q06. Perhaps more importantly, because our model precisely relates Fom b’s mass to its orbit, it can be used to determine the former once the latter is astrometrically secured by imaging at future epochs. Our model is simple, robust to uncertainties in input parameters, and readily applied to other systems.

In §2 we present an overview of the Fomalhaut belt, estimating its physical properties to order-of-magnitude accuracy. These estimates inform our choices for the input parameters of our numerical model; that model, and its output, are detailed in §3. We summarize and discuss our results—describing also the curious anomalous acceleration of Fomalhaut measured by the Hipparcos satellite, and how other planetary companions in addition to Fom b affect our conclusions—in §4.

2. ORDERS OF MAGNITUDE

We derive basic properties of the Fomalhaut dust belt, working as much as possible from first principles and direct observations. The conclusions reached in the following subsections form the basis of our numerical model in §3.

2.1. Bound dust grains present absorbing, geometric cross sections

Fomalhaut is a spectral type A star of luminosity $L_* = 16L_{\odot}$, mass $M_* \approx 2.3M_{\odot}$, and age $t_{\text{age}} = 200 \pm 100$ Myr (Barrado y Navascues et al. 1997; Barrado y Navascues 1998). The circumstellar debris emits a fractional infrared excess of $L_{\text{IR}}/L_* = 4.6 \times 10^{-5}$ (Song et al. 2001). K05 report that from 0.6 to 0.8 μm wavelengths, the ring has a spatially integrated apparent magnitude of $m_{\text{app}} = 16.2$, nearly entirely due to reflected starlight; for the star, $m_{\text{app},*} = 1.12$; therefore the fractional reflected luminosity is $L_{\text{ref}}/L_* \approx 10^{-6}$. If we ignore order unity effects introduced by anisotropy in the scattering phase function (see K05 for a fit to this phase function), the dust albedo is of order $L_{\text{ref}}/L_{\text{IR}} \approx 0.02$ —the grains are nearly purely absorbing.

Dust is generated by the collisional comminution of larger parent bodies. The largest parent bodies sit at the top of the collisional cascade and have lifetimes against collisional disruption equal to t_{age} . We take these largest parents to occupy a torus of radius $R \approx 140$ AU, annular width $\Delta R < R$, and uniform vertical thickness $2H < R$. Strubbe & Chiang (2006) refer to this torus as the “birth ring.” In principle, a grain of given size that is born into the torus is lost from it in one of four ways: collisional comminution, expulsion by radiation pressure, ejection by planetary scattering, or orbital decay by Poynting-Robertson (PR) drag. In practice, for many debris disks, the first two channels are more important than the fourth (Wyatt 2005; Strubbe & Chiang 2006; Thébaud & Wu 2008). The ratio of the force of radiation pressure to that of stellar gravity is

$$\beta = \frac{3L_*}{16\pi cGM_*\rho s} \quad (2)$$

for a geometrically absorbing grain of internal density $\rho \approx 1 \text{ g cm}^{-3}$ and radius s , where c is the speed of light and G is the gravitational constant. Grains are unbound from the star when $\beta \gtrsim 1/2$,⁶ i.e., when

$$s < s_{\text{blow}} \approx \frac{3L_*}{8\pi cGM_*\rho} = 8 \mu\text{m}. \quad (3)$$

Because s_{blow} is much greater than the submicron wavelengths at which the star principally emits, cross sections for absorption of radiation by bound grains are indeed practically geometric, as (2) assumes.

2.2. Radiation Pressure Delivers Grains onto Eccentric, Long-Period Orbits

Upon release from parent bodies moving on circular orbits, bound grains move on orbits of eccentricity

$$e = \frac{\beta}{1 - \beta} = \frac{s_{\text{blow}}}{2s - s_{\text{blow}}} \quad (4)$$

and semimajor axis

$$a = \frac{R}{1 - e}. \quad (5)$$

These expressions, which serve only to guide and which are not used in our more precise numerical models, ignore the parent-grain relative velocities with which grains are born, and also any eccentricity in the parent body orbit. Neither of these errors is serious for the large grain eccentricities of interest here ($e \gtrsim 1/3$; see §2.5). The main point is that radiation pressure flings smaller bound grains born in the torus onto more eccentric, longer period orbits.

2.3. Collisions Between Grains Are Destructive

Colliding belt particles will chip and shatter one another. For an angular orbital velocity Ω_R at semi-major axis R , the relative velocity between grains is at least as large as the vertical velocity dispersion, $\sim H\Omega_R = 100$ m/s. To place this velocity into some perspective, we

⁶ The critical value of $\beta = 1/2$ applies strictly to dust grains released from parent bodies that move initially on circular orbits. For dust grains released from parent bodies moving on mildly eccentric orbits, as is the case in Fomalhaut’s eccentric belt, the critical β varies with the longitude of release, but is still near 1/2.

note that it is comparable to the maximum flow speeds of commercial sandblasting machines.⁷

As a consequence of radiation pressure, many of the grains will be travelling on bound orbits having eccentricities on the order of unity (§2.2). Accounting for orbital eccentricities (in-plane velocity dispersion) only increases collision velocities, up to a maximum given by the local Kepler speed of $R\Omega_R = 4$ km/s. This maximum is comparable to elastic wave speeds in rock and will result in catastrophic shattering.

2.4. Optical Depths: Radial and Vertical

Since the grains present largely geometric cross sections for absorption of starlight, L_{IR}/L_* equals the fraction of the celestial sphere, centered on the star, that is subtended by dust grains:

$$\frac{L_{\text{IR}}}{L_*} = \frac{2\pi R \times 2H \times \tau_R}{4\pi R^2} = \frac{H}{R} \tau_R, \quad (6)$$

where $\tau_R \ll 1$ is the radial geometric optical depth through the torus. K05 give a model-dependent aspect ratio of $H/R = 0.025$; then $\tau_R = 1.8 \times 10^{-3}$.

The vertical optical depth (measured perpendicular to the belt midplane) is

$$\tau_{\perp} = \tau_R \frac{2H}{\Delta R} = \frac{L_{\text{IR}}}{L_*} \frac{2R}{\Delta R}, \quad (7)$$

independent of H . Again from the scattered light observations, $\Delta R/R \approx 0.17$ (K05), whence $\tau_{\perp} = 5.4 \times 10^{-4}$.

2.5. Observable Grains in Fomalhaut's Belt are Bound, and Their Lifetime is Set by Collisions, Not by PR Drag

Unbound grains, for which $\beta \gtrsim 1/2$, exit the torus after a local dynamical time,

$$t_{\text{esc}}(s < s_{\text{blow}}) \sim \frac{1}{\Omega_R} \sim 200 \text{ yr}. \quad (8)$$

Because the lifetime of unbound grains, t_{esc} , is much shorter than the lifetime of bound grains—the latter lifetime is set by collisional disruption; see equation (9) below—the steady-state population of bound grains will be proportionately greater than the unbound population. Combining this fact with the tendency for grain size distributions to concentrate their collective geometric cross section at the smallest sizes, we posit that bound grains near the blow-out size, say $s_{\text{blow}} < s \lesssim 2s_{\text{blow}}$, are responsible for much of the observed scattered light. This view is consistent with the discussion of particle sizes by K05.

Such grains occupy eccentric orbits, $e > 1/3$, and are disrupted by collisions amongst themselves. The lifetime against collisional disruption is

$$t_{\text{col}}(s_{\text{blow}} < s \lesssim 2s_{\text{blow}}) \sim \frac{1}{\Omega(a)\tau} \sim \frac{1}{\Omega_R \tau_R} \left(\frac{\Delta R}{R} \right)^{1/2} \times \frac{1}{(1-e)^{3/2}} \sim 7 \times 10^4 \left(\frac{2/3}{1-e} \right)^{3/2} \text{ yr}, \quad (9)$$

where the effective optical depth $\tau \sim \tau_R(R/\Delta R)^{1/2}$ accounts for the path length $\sim (R\Delta R)^{1/2}$ traversed by a grain on a highly elliptical orbit through the birth ring, where densities are highest and collisions most likely occur. Use of this path length assumes that relative grain velocities are of order the local Kepler velocity; this is an acceptable approximation for the order unity eccentricities of interest here. Account of the limited fraction of time spent within the torus has also been made, via $\Omega(a)$ and (5).

Compare t_{col} with the Poynting-Robertson drag time,

$$t_{\text{PR}}(s_{\text{blow}} < s \lesssim 2s_{\text{blow}}) = \frac{4\pi c^2 \rho}{3L_*} E(e) R^2 s \sim 2.5 \times 10^7 \times \left(\frac{s}{2s_{\text{blow}}} \right) \left(\frac{2/3}{1-e} \right)^{1/2} \text{ yr}, \quad (10)$$

which is the time for an orbit of initial periastron R and initial eccentricity e to shrink to a point (Wyatt & Whipple 1950). This is of the same order as the time for a grain to have its pericenter be dragged out of the birth ring, for ΔR not much less than R , which is the case here. The dimensionless function $E(e > 1/3) > 1.9$ quantifies the decay of orbital eccentricity, and diverges as $(1-e)^{-1/2}$. Comparison of (9) with (10) shows that as long as e is not too close to one—i.e., for all particle sizes outside a tiny interval that just includes s_{blow} —grains are removed from the ring by collisionally cascading down to the blow-out size, and PR drag presents only a minor loss mechanism. In other words, Fomalhaut's disk is Type B or collision-dominated (Strubbe & Chiang 2006).

Our estimate of the collisional lifetime t_{col} in (9) informs the duration of our dust particle simulations, introduced in §3.1.2.

2.6. Total Dust Mass Versus Total Parent Body Mass

The mass M_d in dust responsible for the scattered light is

$$M_d \sim \frac{8\pi}{3} \rho s \tau_{\perp} R \Delta R \sim 10^{-3} M_{\oplus} \left(\frac{s}{2s_{\text{blow}}} \right). \quad (11)$$

The mass M_{pb} in the largest parent bodies at the top of the collisional cascade is given by the steady-state condition

$$\frac{M_{\text{pb}}}{t_{\text{age}}} \approx \frac{M_d}{t_{\text{col}}} \quad (12)$$

which implies

$$M_{\text{pb}} \sim 3M_{\oplus}.$$

This is a minimum mass for the disk as a whole because still larger bodies may exist which are collisionless over t_{age} .

Some workers (e.g., Backman & Paresce 1993) calculate the mass in parent bodies by explicitly assuming a size distribution appropriate for an idealized collisional cascade (Dohnanyi 1969) and taking the upper size to be some value > 1 km. Not only is it unnecessary to specify a size distribution, but it is not justified to adopt a specific value for the parent body size without first establishing that a typical such body can be collisionally disrupted within the finite age of the system. The super-kilometer sizes often invoked (e.g., K05) fail this test.

⁷ See, e.g., <http://www.nauticexpo.com/boat-manufacturer/sandblasting-machine-19911.html>.

3. NUMERICAL MODEL

We devise a dynamical model of the Fomalhaut planet-belt system that reproduces approximately some of the properties inferred from the HST observations. We compute the shape of the vertical optical depth profile, $\tau_{\perp}(a)$, of dust particles in the belt and match this profile against that of the K05 scattered light model. We seek in particular to find those combinations of planet mass and orbit that yield an inner edge to the belt of $a_{\text{inner}} = 133$ AU.

The procedure is detailed in §3.1; results are given in §3.2; and extensions of the model, including some validation tests, are described in §3.3.

3.1. Procedure

Our numerical modeling procedure divides into four steps, described in the following four subsections, §§3.1.1–3.1.4. In short, we (1) create a population of parent bodies that is stable to gravitational perturbations from Fom b over t_{age} ; (2) release dust particles from stable parent bodies and follow dust trajectories in the presence of radiation forces over the collisional lifetime t_{col} ; (3) compute the optical depth profile $\tau_{\perp}(a)$ of dust particles at the end of t_{col} , accounting for their size distribution; and (4) compare with the K05 scattered light model, which serves as our proxy for the observations.

3.1.1. Step 1: Create Stable Parent Bodies

Parent bodies (a) execute orbits that are stable to gravitational perturbations over t_{age} , (b) occupy the top of the collisional cascade, which by definition implies that their orbits are little affected by catastrophic collisions for times $t < t_{\text{age}}$, and (c) are large enough that radiation forces are negligible. We assume further that (d) the self-gravity of the belt is negligible. Thus the problem of simulating a realistic parent body is a purely gravitational, three-body problem involving the star, planet, and exterior parent body, where the parent body is treated as a test particle. Finding stable test particle orbits is a straightforward matter of specifying their initial conditions, integrating the equations of motion forward for $\sim t_{\text{age}}$, and selecting those particles that survive the integration.

Integrations of parent bodies are performed with the `swift_whm` code, written by H. Levison and M. Duncan (www.boulder.swri.edu/~hal/swift.html) using the Wisdom & Holman (1991) algorithm. We set the stellar mass $M_* = 2.3M_{\odot}$. In each of our five mass models, a planet of mass $M_{\text{pl}} \in (0.1, 0.3, 1, 3, 10)M_J$ resides on a (fixed) elliptical orbit of semimajor axis a_{pl} and eccentricity e_{pl} . These quantities are listed in Table 1 (placed at the end of this manuscript); see below for how we relate e_{pl} to a_{pl} , and Step 4 (§3.1.4) for how we select a_{pl} given M_{pl} . The planet’s orbital plane defines the x - y reference plane for the system. The planet’s longitude of periastron $\tilde{\omega}_{\text{pl}} = 0$. At the start of the integration, the planet is located at periastron. All orbital elements reported here are stellocentric and osculating unless otherwise noted.

Each run begins with $N_{\text{tp}} = 10^4$ test particles and lasts 10^8 yr. Particles are discarded as “unstable” if either they approach within a Hill sphere $R_{\text{H}} = (\mu/3)^{1/3}a_{\text{pl}}$ of the planet, or their distance from the star exceeds 1000 AU, as a result of gravitational scatterings off the planet. Particles that survive until the end of the run are deemed

“stable” and are used in subsequent steps of our procedure. The integration timestep is 15000 days, equivalent to 5–7% of the planet’s orbital period, depending on the model.

Initial conditions for test particles are as follows. Initial semimajor axes a are distributed systematically and uniformly between 120 AU and 140 AU (for the 0.1 M_J model, the starting particle semimajor axis is 125 AU since the planet semimajor axis turns out to be $a_{\text{pl}} = 120$ AU). Initial eccentricities are set equal to the forced values given by the classical, linear, secular theory of Laplace-Lagrange (L-L):

$$e(a) = e_{\text{forced}}(a) = \frac{b_{3/2}^{(2)}(a_{\text{pl}}/a)}{b_{3/2}^{(1)}(a_{\text{pl}}/a)}e_{\text{pl}} \quad (13)$$

where the b ’s are the usual Laplace coefficients (e.g., Murray & Dermott 2000). Initial inclinations i of test particles are drawn randomly from a uniform distribution between 0 and 0.025 rad.⁸ Our maximum inclination matches the opening angle of the K05 scattered light disk model. Initial longitudes of periastron of all particles equal the secularly forced value $\tilde{\omega} = 0$, corresponding to apsidal alignment with the planet; longitudes of ascending node $\tilde{\Omega}$ are drawn randomly from a uniform distribution between 0 and 2π ; and arguments of periastron $\omega = -\tilde{\Omega}$ (so that $\tilde{\omega} = 0$). Finally, initial mean anomalies M are drawn randomly from a uniform distribution between 0 and 2π .

For a given a_{pl} in a given model, the planet’s eccentricity e_{pl} is such that a test particle at $a = 140.7$ AU acquires a secularly forced eccentricity of $e = 0.11$, as computed using (13). Such parameters are inspired by the elliptical orbit fitted by K05 to the brightest portions of the belt. The planetary eccentricity so chosen is about $e_{\text{pl}} = 0.12$, varying by up to 15% between our five models (see Table 1).

According to L-L, the initial conditions so prescribed produce test particle orbits whose eccentricity vectors $\mathbf{e} = (e \cos \tilde{\omega}, e \sin \tilde{\omega})$ are purely forced; they have and will have no free component (e.g., Murray & Dermott 2000). As such, because the planet’s orbit is fixed, belt particle orbits also should not vary, at the L-L level of approximation.⁹ In §3.2.4, we describe the extent to which this expectation is borne out.

Our initial conditions, which comprise nested, apsidally aligned, purely forced elliptical orbits, are designed to reproduce the observed elliptical belt of Fomalhaut (Wyatt et al. 1999; Quillen 2006). However, such forced orbits are not the only ones that are stable in the vicinity

⁸ Such an inclination distribution is unphysical because in reality, there is zero probability density for finding an object with zero inclination. Nevertheless, we adopt our boxcar distribution for simplicity.

⁹ Laplace-Lagrange truncates the secular disturbing function at $O(e^2, i^2)$ and so in reality and in numerical integrations, the eccentricities and apsidal angles are still expected to vary somewhat with time with our initial conditions, even if the system were purely secular. One can avoid such truncation error by employing Gauss’s perturbation equations for \dot{e} and $\dot{\tilde{\omega}}$ and integrating the planetary forces over Gaussian wires (e.g., Murray & Dermott 2000), thereby finding exact forced eccentricities for which $\dot{e} = \dot{\tilde{\omega}} = 0$. We skip this refinement, in part because the system is not purely secular; nearby mean-motion resonances influence the dynamics.

of Fom b. In §3.3.3, we experiment with a different set of initial conditions that generate another class of stable parent body.

3.1.2. Step 2: Integrate Dust Trajectories

Having created an ensemble of stable parent bodies, we now model the dust generated by such bodies. At the end of a 10^8 -yr-long integration from Step 1, we take each stable parent body and have it “release” a dust grain with the same instantaneous position and velocity as its parent’s. Each dust grain’s trajectory is then integrated forward under the effects of radiation pressure and PR drag. That is, in addition to the gravitational accelerations from the star and the planet, a dust particle also feels a radiative acceleration (see, e.g., Burns et al. 1979)

$$\mathbf{a}_{\text{rad}} = \frac{GM_*\beta}{r^2} \left(\hat{\mathbf{r}} - \frac{v_r\hat{\mathbf{r}} + \mathbf{v}}{c} \right) \quad (14)$$

where $\mathbf{r} = r\hat{\mathbf{r}}$ is the vector displacement from the star to the grain, \mathbf{v} is the velocity of the grain relative to the star, and $v_r = \mathbf{v} \cdot \hat{\mathbf{r}}$ accounts for the Doppler shift in stellar radiation seen by the grain. We add this radiative acceleration to the Bulirsch-Stoer (B-S) integrator `swift_bs`, written by Levison & Duncan. We prefer to modify the B-S integrator over the Wisdom-Holman integrator, since the latter is designed to model a dissipationless Hamiltonian system; when PR drag is included, the system is dissipative, and it is not obvious to us how we should add the radiative perturbations to the symplectic kick-drift-kick algorithm. (Nevertheless, adding radiative forces to symplectic integrators is standard practice in the literature and has been shown to produce accurate results.) Though the B-S integrator is slower, it is fast enough for our purposes since our integration times for Step 2 are short (see below). The accuracy parameter “eps” of `swift_bs` is set to 10^{-8} . The modified code was tested on test particles having various β ’s, producing results for radiation blow-out and PR drag in excellent agreement with analytic and semi-analytic studies (e.g., Wyatt & Whipple 1950).

From each of the five parent body integrations completed in Step 1, we generate eight dust simulations in Step 2, each characterized by a single value of $\beta \in (0, 0.00625, 0.0125, 0.025, \dots, 0.4)$. Dust grains released with such β ’s are mostly still bound to the star, albeit on highly eccentric orbits for β approaching 0.4. Bound grains contribute substantially, if not predominantly, to the scattered light observations: as sketched in §2, because $t_{\text{PR}} \gg t_{\text{col}} \gg t_{\text{esc}}$, the lifetime of bound grains is set by destructive interparticle collisions, not by PR drag, and the steady-state population of bound grains greatly outweighs that of unbound grains, by $t_{\text{col}}/t_{\text{esc}}$.

Because the dust lifetime is set by collisions, we extract dust grain orbits for further analysis in Step 3 after integrating for a time t_{col} . Following our order-of-magnitude estimate (9), we set $t_{\text{col}} = 10^5$ yr. During the integration, we discard particles that approach within a Hill sphere of the planet or whose distances from the star exceed 10000 AU (this is a factor of 10 larger than the cut imposed in Step 1, because large apastron distances result from the onset of radiation pressure and do not necessarily imply orbital instability). As Table 1 indicates, few if any dust particles are discarded in our β -simulations, with the exception of our $10 M_J$ model.

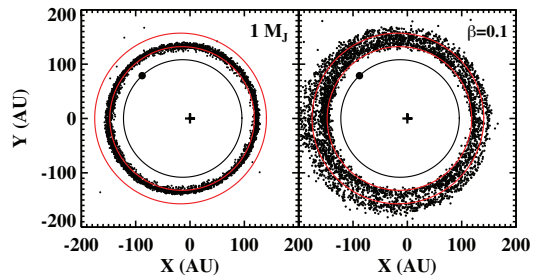


FIG. 1.— Snapshots of parent bodies (left) and $\beta = 0.1$ dust grains (right), for our $1M_J$ model. The cross marks Fomalhaut, while the solid circle marks Fomalhaut b. Parent bodies are imaged after an integration time of $t_{\text{age}} + t_{\text{col}}$. Dust particles are released from parent bodies with zero relative velocity after t_{age} and their trajectories integrated forward with $\beta = 0.1$ for t_{col} . Red ellipses correspond to the inner and outer boundaries of the K05 scattered light model ($a_{\text{inner}} = 133$ AU, $a_{\text{outer}} = 158$ AU, $e = 0.11$). Radiation pressure spreads dust particles outward from where they were born, but leaves their inner boundary practically coincident with that of parent bodies.

In §3.3.2, we test the sensitivity of our results to t_{col} , whose value we know only to within factors of a few. In that subsection we also examine whether our results change significantly if we model the dust more realistically by releasing grains gradually over t_{col} .

Figure 1 provides sample snapshots of dust grains and their parent bodies projected onto the x - y plane, for our $1M_J$ model.

3.1.3. Step 3: Compute Optical Depth Profile

If we had a sufficiently large number of dust particles, we could simply take a snapshot of each Step 2 β -simulation after t_{col} and count the number of dust particles per unit x - y area of the belt. We would thereby measure the surface density $N_{\beta}(x, y)$, and by extension the vertical optical depth $\tau_{\perp}(x, y)$. In practice, we do not have enough particles, and such an exercise produces noisy results.

We greatly improve the signal-to-noise by spreading each dust particle along its orbit according to how much time it spends traversing a given segment of its orbit. In other words, we replace each dust particle with its equivalent Gaussian wire, and measure the optical depth presented by the collection of wires. We refer the Kepler elements of a dust particle’s orbit to $(1 - \beta)$ times the stellar mass; otherwise the elements would not remain constant in a two-body approximation.

First we construct an eccentric grid by partitioning the x - y plane into a series of nested, confocal ellipses, all having the same eccentricity of 0.11 (K05), and having semimajor axes running uniformly from $a_1 = 100$ AU to $a_N = 220$ AU in steps of $\Delta a = 0.5$ AU. Our goal is to measure $\tau_{\perp}(a_i)$, the average optical depth between the i^{th} ellipse having semimajor axis a_i and the $(i + 1)^{\text{th}}$ ellipse having semimajor axis $a_{i+1} = a_i + \Delta a$. Each dust particle orbit is divided into 1000 segments spaced uniformly in true anomaly from 0 to 2π . Each segment maps to a certain location on the grid (i.e., the x - y position of each segment falls between two adjacent ellipses on the grid). Associated with each segment is an orbital weight, equal to the fraction of the orbital period spent traversing that segment (the sum of all orbital weights for a given particle/orbit equals one). The orbital weight for

each segment is added to its grid location. This process is repeated over all segments of all orbits. Finally, at each grid location a_i , the sum of orbital weights is divided by the area of the annulus extending from the i^{th} ellipse to the $(i + 1)^{\text{th}}$ ellipse. This yields the relative surface density profile $N_\beta(a_i)$, for a simulation characterized by β .

The various N_β profiles for our $1M_J$ model are plotted in the top panel of Figure 2. The profiles are normalized to the peak of the N_0 ($\beta = 0$) profile. Since the number of dust particles is practically constant across all β -simulations within a given mass model (Table 1), the decreasing height of each N_β profile with increasing β simply reflects how dust particle orbits become increasingly eccentric and elongated with increasing β (cf. equation 4). In other words, the same number of particles is being spread into a disk that extends farther out the greater the radiation pressure. At the same time, the peaks of the N_β profiles hardly move with increasing β : as long as the grain is still bound to the star, it must always return to the same stellocentric distance at which it was released, no matter how strongly it feels radiation pressure. That release distance is located in the birth ring (Strubbe & Chiang 2006) or, more accurately, the birth ellipse of parent bodies, near $a \approx 130\text{--}140$ AU; see the left-hand panel of Figure 1.

Once all the N_β profiles are in hand, we combine them linearly to produce the total optical depth profile τ_\perp :

$$\tau_\perp = \sum_{\beta \neq 0} N_\beta \frac{\max N_{0.00625}}{\max N_\beta} \left(\frac{\beta}{0.00625} \right)^{q-3} + N_0 \frac{\max N_{0.00625}}{\max N_0} (1 + \sqrt{2}). \quad (15)$$

The rationale behind this formula is as follows. As Figure 2 indicates, the maxima of the N_β profiles are all situated in the birth ring. Following Strubbe & Chiang (2006), we posit that the size distribution of grains in the birth ring is given by a Dohnanyi (1969) cascade, with differential power-law index $q = 7/2$. For such a power-law size distribution, the collective surface area or geometric optical depth, evaluated per logarithmic bin in β , scales as β^{q-3} ($\propto s^{3-q}$). The two factors multiplying N_β in the sum in (15) enforce this scaling in the birth ring (whose location is traced by the maxima of the surface density profiles), and we have adopted the $\beta = 0.00625$ bin as our reference bin.

The last term proportional to N_0 accounts for the optical depth contributed by grains having $0 < \beta < 0.00625$. We take the surface density profile of such grains to be given by N_0 ; this is a good approximation, as there is little difference between $N_{0.00625}$ and N_0 (Figure 2, top panel). Since our grid of models for $\beta \geq 0.00625$ is logarithmic in β —successive bins are separated by factors of $B = 2$ —we extend the same logarithmic grid for $\beta < 0.00625$. Then the optical depth coming from all grains having $\beta < 0.00625$, scaled to the optical depth in our $\beta = 0.00625$ reference bin, is $\sum_{j=1}^{\infty} (1/B)^{j(q-3)} = 1 + \sqrt{2}$.

3.1.4. Step 4: Compare with Observations

A rigorous comparison with observations would require us to produce a scattered light image based on our dy-

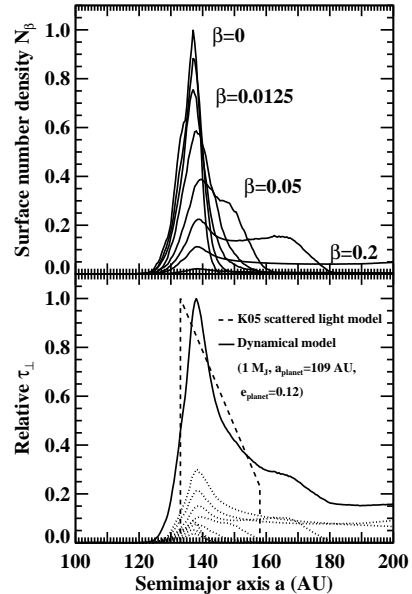


FIG. 2.— *Top panel:* Surface density profiles of dust grains for our $1M_J$ model, computed $t_{\text{col}} = 10^5$ yr after release, normalized to the peak of the $\beta = 0$ curve. These profiles are computed by binning wire segments on a fixed elliptical grid, as described in the main text under Step 3 of our procedure. Profiles shrink vertically and widen horizontally with increasing β , reflecting how increased radiation pressure spreads particles outward by amplifying apastron distances. By contrast, periastron distances are more nearly conserved for bound particles, since they always return to the birth ring regardless of the strength of radiation pressure. Thus the peaks of the N_β profiles, which mark the location of the birth ring of parent bodies (see left panel of Figure 1), hardly shift with β . *Bottom panel:* Vertical optical depth profile (solid line) obtained by adding together the individual N_β profiles (dotted lines), appropriately weighted according to a Dohnanyi size distribution (see equation 15). At $a \lesssim 160$ AU, the profile resembles that of the K05 scattered light model (dashed line), which itself is an approximate, idealized, and non-unique representation of the HST observations. Discrepancies at large $a \gtrsim 160$ AU are expected, in large part because the HST images are too noisy to usefully constrain the K05 model there.

namical model. This is a considerable task. Our τ_\perp profile, combined with the vertical density distribution and a grain scattering phase function, would be used to calculate the direction-dependent emissivity of the belt as a function of 3D position. This emissivity model would then be ray-traced at a non-zero viewing angle to produce a model scattered light image. Various parameters (e.g., normalization of τ_\perp , grain scattering asymmetry parameter, viewing angle) would need to be adjusted, including input parameters from Steps 1–3 (distribution of initial semimajor axes, distribution of initial inclinations), to produce a good subtraction of the observed image.

In this first study, we attempt none of this. Instead we compare the τ_\perp profile given by (15) with the corresponding optical depth profile of the K05 scattered light model, focussing on the one belt property that seems most diagnostic of planet mass and orbit: the belt’s inner edge. The K05 optical depth profile extends from $a_{\text{inner}} = 133$ AU to $a_{\text{outer}} = 158$ AU and falls as $a^{-8.5}$ (their fitted volumetric number density of grains falls as a^{-9} , while the fitted vertical thickness of the belt increases as $a^{0.5}$). In our dynamical modeling, for given

planet mass M_{pl} , we adjust only the planet semimajor axis a_{pl} and repeat Steps 1–3 until the minimum semimajor axis at which τ_{\perp} reaches half its maximum value—the “half-maximum radius”—equals $a_{\text{inner}} = 133$ AU.

Since our dynamical models are anchored to a_{inner} , we should have a sense of the uncertainty in this parameter. The K05 model is based on fits “by eye.” From the visual fits, the uncertainty is about ± 1 AU, slightly larger than the size of a 2-pixel resolution element (0.1 arcsecond or 0.77 AU; the images are binned 2×2 before they are modeled, to increase signal-to-noise). The error in a_{inner} propagates into our constraints on planet mass.

It is well to appreciate that while our general goal is to reproduce the shape of the optical depth profile of the K05 scattered light model, that model is itself highly idealized, characterized by knife-edge sharp inner and outer edges and simple power-law behavior. Fitting by eye means the model is at best approximate. And as K05 caution, only a restricted azimuth of the belt (near their quadrant “Q2”) was analyzed in detail to produce their fit parameters. Therefore we should neither aim for, nor expect, perfect agreement between our dynamical model and the K05 model. Our task instead is to use the K05 model as a guide, to identify robust trends and to rule out those regimes of parameter space for Fom b that give blatantly poor agreement with observation.

Lastly, neither our dynamical model nor the K05 scattered light model should be trusted at large $a \gtrsim 160$ AU. At large distance, barely bound grains whose β ’s are arbitrarily close to the blow-out limit of ~ 0.5 dominate τ_{\perp} . Our set of 8 β -simulations lacks the resolution in β to accurately model this outer disk (see Strubbe & Chiang 2006 for an analytic treatment appropriate for a circular birth ring). Observationally, the HST images at stellocentric distances $\gtrsim 158$ AU are dominated by the sky background; see Figure 3 of K05.

3.2. Results

In §3.2.1 we give an approximate formula relating the planet mass to the width of the chaotic zone, based on our five mass models. In §3.2.2, we compare our optical depth profiles with that of the K05 scattered light model. Based on this comparison we argue against large planetary masses for Fom b. In §3.2.3 we argue the same point by comparing our model planetary orbits with the observed stellocentric distance of Fom b. Finally, the underlying dynamics of parent bodies and of dust particles is discussed briefly in §3.2.4.

3.2.1. Chaotic Zone Width

In Figure 3, we overlay the τ_{\perp} profiles of our five mass models together with the optical depth profile of the K05 scattered light model. As described in §3.1.4, the planet semimajor axis a_{pl} for each mass model is chosen such that the “half-maximum radius”—the smallest semimajor axis at which τ_{\perp} attains half its peak value—equals K05’s $a_{\text{inner}} = 133$ AU. The a_{pl} ’s so determined are listed in Table 1 and also annotated on Figure 3. They are such that the semimajor axis separation between belt inner edge and planet is given by

$$a_{\text{inner}} - a_{\text{pl}} = 2.0 \mu^{2/7} a_{\text{pl}}, \quad (16)$$

with less than 6% variation in the coefficient across mass models, and where $a_{\text{inner}} = 133$ AU. Because we are

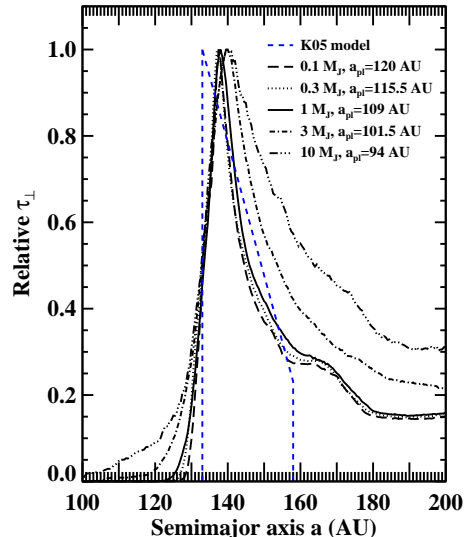


FIG. 3.— Vertical optical depth profiles of our five mass models (black lines), overlaid with that of the K05 scattered light model (blue dashed line). Parameters for our dynamical models are listed in the inset and are such that the “half-maximum radius”—the minimum semimajor axis for which τ_{\perp} attains half its maximum value—equals 133 AU, the innermost semimajor axis of the K05 model. Models for which $M_{\text{pl}} \leq 1M_J$ do equally well in reproducing the K05 model. As M_{pl} increases, the τ_{\perp} profiles widen because the planet increasingly perturbs dust grains onto eccentric orbits. The $10M_J$ model is probably unacceptably wide. At $a \gtrsim 160$ AU, neither the dynamical model nor the K05 model is trustworthy; the former suffers from poor resolution in β , while the latter is limited by sky background (see Figure 3 of K05).

connecting more directly to the HST observations, our Fomalhaut-specific coefficient of 2.0 is preferred over the smaller coefficients cited by previous works; accuracy matters for determining planet mass, whose value scales strongly as the $7/2$ power of distance measurements. Measured in Hill radii (evaluated using a_{pl}), the separation $a_{\text{inner}} - a_{\text{pl}}$ ranges from 3.7 to 4.5 R_H in order of decreasing M_{pl} .

3.2.2. Comparison of τ_{\perp} Profiles Implies $M_{\text{pl}} < 3M_J$

What resemblance there is in Figure 3 between dynamical and scattered light τ_{\perp} profiles leads us to believe that we are on the right track towards understanding the underlying properties of the Fomalhaut planet-belt system. We are especially encouraged when we consider that with the exception of a_{pl} , none of our model parameters (e.g., grain size index q , distribution of initial semimajor axes) has been adjusted from its naive standard value. And as we emphasized at the end of §3.1.4, the K05 scattered light model is itself highly idealized and approximate, and does not represent a unique model of the observations. In particular, the K05 model idealizes the inner edge as a step function, but smoother profiles also seem possible; the degree of smoothness may help to constrain q .

Discrepancies at large $a \gtrsim 160$ AU are not serious, since both the dynamical and scattered light models are known to fail there (§3.1.4). The deficiency in our dynamical model can be remedied by having a finer grid in β near the blow-out value of ~ 0.5 , while improvements in the

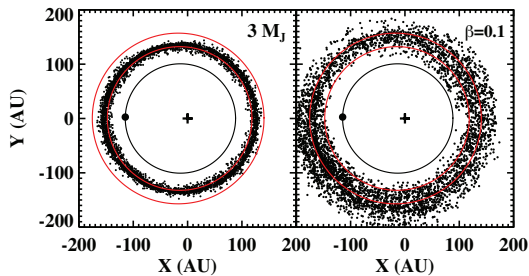


FIG. 4.— Snapshots of parent bodies (left) and $\beta = 0.1$ dust grains (right), for our $3M_J$ model. Compare with the $1M_J$ model shown in Figure 1. The larger the planet mass, the more dust particles are perturbed by the planet into a more spatially extended disk.

scattered light model await deeper imaging campaigns.

As M_{pl} increases, the τ_{\perp} profiles broaden—see in particular the curve for $10M_J$. Upon release, dust particles find themselves in a weakened stellar potential because of radiation pressure. More massive planets more readily perturb dust onto more eccentric orbits that extend both inside and outside of the birth ring. This is further illustrated in Figure 4, which shows a snapshot of $\beta = 0.1$ grains for $M_{\text{pl}} = 3M_J$. Moreover, as documented in Table 1, planetary perturbations are so severe for our $10M_J$ model that about 1/3 of the dust particles launched with $\beta = 0.05$ are discarded as unstable within $t_{\text{col}} = 10^5$ yr. (Why $\beta = 0.05$? Larger β grains are, upon release, repelled immediately away from the planet onto highly eccentric trajectories by radiation pressure alone and are therefore less likely to be rendered unstable by the planet. Smaller β grains share essentially the same stability properties as the parent bodies.)

The τ_{\perp} profile for $M_{\text{pl}} = 10M_J$ is probably unacceptably broad: at $140 \text{ AU} \lesssim a \lesssim 160 \text{ AU}$, the dynamical model predicts too large an optical depth compared to the K05 model, by about a factor of two. At these distances, a factor of two overluminosity in the belt is not easily accommodated, as judged from the error bars on the observed surface brightness profile—see Figure 3 of K05. This same $10M_J$ model also produces a tail extending inward to $a \lesssim 120 \text{ AU}$, but the observations, whose dynamic range in surface brightness is limited to less than 10:1 (see Figure 3 of K05), probably cannot rule out such a feature. We have verified that the excessively large τ_{\perp} at $a \gtrsim 140 \text{ AU}$ follows primarily from the large eccentricities acquired by $\beta \approx 0.2\text{--}0.4$ dust particles from planetary perturbations. By contrast, the $M_{\text{pl}} \leq 1M_J$ models, which produce practically identical τ_{\perp} profiles, appear compatible with the K05 model, given the various limitations of the latter.

The low-mass models having $M_{\text{pl}} \leq 1M_J$ have inner edges that are practically identically sharp. A measure of the sharpness is the distance over which τ_{\perp} rises from the half-maximum radius to the semimajor axis at which τ_{\perp} peaks, normalized by the half-maximum radius. This fractional distance is $\delta = 4.5 \text{ AU}/133 \text{ AU} = 0.034$. Quillen (2006) recognizes that in fitting the observed drop-off in surface brightness for a belt that is inclined to our line of sight, a trade-off exists between the belt’s vertical and radial density profiles. Either the belt can have a finite vertical thickness and be knife-edge sharp in the

radial direction (as in the K05 scattered light model); or have zero vertical thickness and drop off gradually in the radial direction; or be characterized by some intermediate combination. In this context, our measure for the fractional radial drop-off distance, $\delta = 0.034$, compares promisingly with the fractional vertical drop-off distance inferred by K05, $2H/R = 0.025$. In the future, we will have to adjust both radial and vertical drop-off distances to better reproduce the scattered light observations. The vertical thickness of the belt appears to be fairly easily adjusted in our model, given that the inclinations of our dust particles are mostly unchanged from the assumed initial inclinations of our parent bodies (see Figure 7 and related discussion in §3.2.4).

In the bottom panel of Figure 2, we plot as dotted curves the separate terms in equation (15) that add up to τ_{\perp} . The terms corresponding to larger β (or smaller grain size $s \propto 1/\beta$) dominate, as a consequence of our assumption that the grain size distribution in the birth ring follows a Dohnanyi law. That law apportions the bulk of the geometric surface area in the smallest grains.

3.2.3. Fom b’s Current Stellocentric Distance Implies $M_{\text{pl}} < 3M_J$

Each of our mass models specifies a certain orbit for Fom b (Table 1) that is tuned, through multiple iterations of Steps 1–4, to generate the observed ellipticity of the belt and to yield a half-maximum radius equal to K05’s $a_{\text{inner}} = 133 \text{ AU}$. If the apocentric distance of a model orbit is less than the observed stellocentric distance of Fom b, then that model can be ruled out.

Currently, only the distance between Fom b and its host star projected onto the sky plane is known. In 2006, that projected distance was 97.6 AU. Inferring the true stellocentric distance requires that we de-project the orbit of Fom b. But with only two epochs of observation, a unique de-projection is not possible. Nevertheless, we can perform a rough de-projection by making a few assumptions. We assume that the planet’s orbit is oriented such that its semimajor axis lies in the plane of the sky and is parallel to the line joining the observed belt ansae. We also assume that the inclination of the planet’s orbit to the sky plane equals 65.6° , the same as that inferred for the belt orbital plane (K05). These assumptions are reasonable. K05 fit and de-project an ellipse to the brightest portions of the belt. They find that the true semimajor axis of the ellipse is not strongly inclined to the line joining the observed belt ansae—see Figure 1 of K05. We expect the same to be true for the planet’s orbit, since it is apsidally aligned with that of the belt.¹⁰ In addition, the mean belt plane should coincide with that of the planet’s orbital plane, by virtue of differential precession of the ascending nodes of individual belt particle orbits.¹⁰

The resultant de-projected stellocentric distance of Fom b in 2006 is 119 AU, with a systematic error of probably no more than a couple AUs. Such a distance argues against our $10M_J$ model, for which the apocen-

¹⁰ Unless there are more planets that significantly alter the eccentricity and inclination evolution of belt particles, in which case our procedure would need to be revised starting at Step 1. More planets may well exist in the Fomalhaut system, but the proximity of Fom b to the belt suggests that Fom b dominates the belt’s dynamics. See also the discussion in §4.

tric distance of Fom b is 107 AU. The discrepancy is depicted in Figure 5. That same figure shows that the $3M_J$ model is also inconsistent, but only marginally so, and without a proper de-projection, we hesitate to rule it out. Lower masses $M_{\text{pl}} \leq 1M_J$ are, by contrast, easily compatible. These findings reinforce those based purely on a comparison of the optical depth profiles (§3.2.2).

3.2.4. Parent Body and Dust Particle Dynamics

In Figure 5, we supply sample histograms of time-averaged semimajor axes of stable parent bodies generated in Step 1. The time average is performed over a 10^5 -yr-long window (with $\beta = 0$) following each 10^8 -yr-long integration. Intriguingly, parent bodies appear evacuated from exterior mean-motion resonances established by Fom b, even outside the planet’s main chaotic zone. The reasons for this are likely analogous to why the solar system’s Kirkwood gaps, located at Jupiter’s interior mean-motion resonances, are empty of asteroids (Wisdom 1982, 1983, 1985). Study of this phenomenon, which depends on the non-zero eccentricity of the planet’s orbit, is deferred to future work.

Figure 6 plots the eccentricity vectors of the parent bodies at the end of 10^8 yr (black points). While they remain clustered near their initially purely forced values, there is a dispersion that is not predicted by L-L: the parent bodies acquire free eccentricities despite having none to start with. The more massive the planet, the greater the free eccentricities that develop. This same behavior was found by Quillen (2006) and Quillen & Faber (2006), who attributed it to forcing by a mean-motion resonance just outside the chaotic zone.

Figure 6 also describes how dust particles (colored points) born from parent bodies acquire free eccentricities. Initial free eccentricity vectors are distributed roughly axisymmetrically about the forced eccentricities. The initial free phase depends on the orbital phase of release. For example, a dust particle released at the parent body’s periastron gains a free eccentricity vector in the $+\hat{\mathbf{k}}$ direction (total eccentricity increases), while release at apastron yields a free eccentricity in the $-\hat{\mathbf{k}}$ direction (total eccentricity decreases, at least for β not too large). Though these radiation-induced free eccentricities of dust grains are much larger than the free eccentricities acquired by parent bodies, they do not necessarily lead to increased blurring of the belt inner edge, because the semimajor axes of dust grains shift correspondingly outward by radiation pressure as well (cf. equation 5). We have verified that the various N_β surface density profiles for $M_{\text{pl}} \leq 1M_J$ have comparably sharp inner edges for all β , as gauged using our fractional width parameter δ . For further discussion of what influences the sharpness of the inner edge, see §3.3.1.

Finally, in Figure 7 we examine how the orbital inclinations of stable parent bodies change after 10^8 yr. Laplace-Lagrange predicts that the mutual inclination between planet and particle is conserved, and indeed most inclinations are little altered from their initial values (which span up to 0.025 rad). Fewer than 10% of all surviving parent bodies have final inclinations that exceed initial inclinations by more than 0.0025 rad. Excited bodies are localized to mean-motion resonances. Even in the vicinity of a resonance, the fraction of bodies that

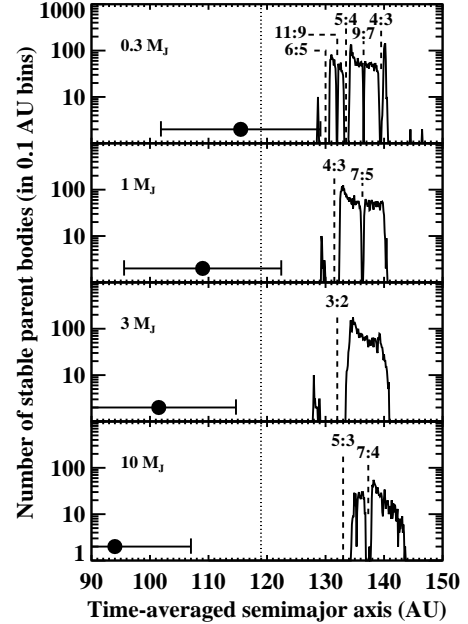


FIG. 5.— Histogram of time-averaged semimajor axes of parent bodies that survive for 10^8 yr in the vicinity of Fom b. The bin width is 0.1 AU, and the time average is performed over 10^5 yr. Each panel corresponds to a different mass model, as annotated. The black circle in each panel marks the semimajor axis of Fom b, with error bars extending from the model orbit’s pericentric distance to its apocentric distance. Only model orbits corresponding to $M_{\text{pl}} \lesssim 1M_J$ are consistent with the estimated de-projected stellocentric distance of Fom b in 2006 (dotted vertical line). Stable parent bodies are located outside the planet’s chaotic zone, at semimajor axes greater than the planet’s by about $2\mu^{2/7}a_{\text{pl}}$. Inside the chaotic zone, first-order mean-motion resonances overlap and particle orbits are short-lived. Outside the chaotic zone, parent bodies reside stably on secularly forced eccentric orbits, with occasional gaps located at mean-motion resonances as indicated. The gaps are evacuated for reasons likely analogous to why the solar system’s Kirkwood gaps are empty of asteroids.

have their inclinations pumped is small. For example, in our $1M_J$ model, only 10% of all stable parent bodies having time-averaged semimajor axes between 132 and 133.1 AU—particles right at the inner edge of the belt, in the vicinity of the 4:3 resonance—have final inclinations exceeding initial inclinations by more than 0.0025 rad. The near constancy of inclination should simplify future modelling efforts: whatever vertical thickness of the belt is desired to match the scattered light images can be input into the dynamical model as an initial condition, in Step 1.

3.3. Extensions and Refinements

In §3.3.1 we reconcile our results on the sharpness of the inner belt edge with those of Q06. In §3.3.2 we examine how robust our optical depth profiles are to uncertainties in t_{col} and to our simplifying assumption that the profile is adequately simulated by releasing grains from parent bodies at a single time. In §3.3.3 we experiment with different test particle initial conditions to see whether they might yield superior fits to the observations.

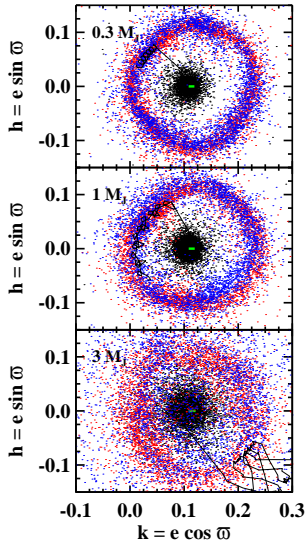


FIG. 6.— Locations in complex eccentricity space of all parent bodies at $t = 0$ (green bar) and those parent bodies that survive for $t = 10^8$ yr (black points). The locus of survivors is not exactly centered on the locus of initial conditions because the survivors are all at large semimajor axes (smaller forced eccentricities), and because of inaccuracies in the L-L theory which was used to determine the initial conditions. Surviving parent bodies remain approximately apsidally aligned with the planet’s orbit, deviating by less than $\pm 15^\circ$ in most cases. The deviations, i.e., the dispersions in free eccentricity, increase with M_{pl} . This same behavior was found by Quillen (2006). However, contrary to that work, we find that the increased dispersion does not necessarily imply a more spatially diffuse inner edge to the belt; see Figure 8 and §3.3.1. Also shown are $\beta = 0.1$ dust particles 10^4 yr after release (red points), and those same dust particles 10^5 yr after release (blue points). The trajectory of a typical dust particle is shown sampled every 10^3 yr, starting from release. Note the large eccentricity variations for the $3 M_J$ model.

3.3.1. Sharpness of Inner Belt Edge

In Figure 3, we found that the sharpness of the belt’s inner edge, as gauged by our measure δ (see §3.2.2), hardly varied with $M_{\text{pl}} \leq 1 M_J$. This finding is seemingly at odds with that of Q06, who gauges sharpness using the velocity dispersion of parent bodies at the boundary of the chaotic zone, and who finds that it increases smoothly as $\mu^{3/7}$. As a consequence of this relation, Q06 concludes that M_{pl} cannot exceed $\sim 7 \times 10^{-5} M_* = 0.2 M_J$ and still have the belt edge be as sharp as the observations imply. Indeed we also found in Figure 6 that the velocity dispersion of parent bodies, as indicated by their spread in free eccentricities, increased smoothly with M_{pl} , in apparent agreement with Q06. Yet the smoothly growing velocity dispersion is not reflected in the relative sharpness of our optical depth profiles across mass models.

How can this be? It might be thought that the discrepancy arises because Q06’s calculation of the velocity dispersion pertains to parent bodies, while our calculation of τ_\perp involves dust. While as a point of principle our calculation would be preferred because the observations are of dust and not of parent bodies, this explanation does not get at the heart of the problem, as we find the

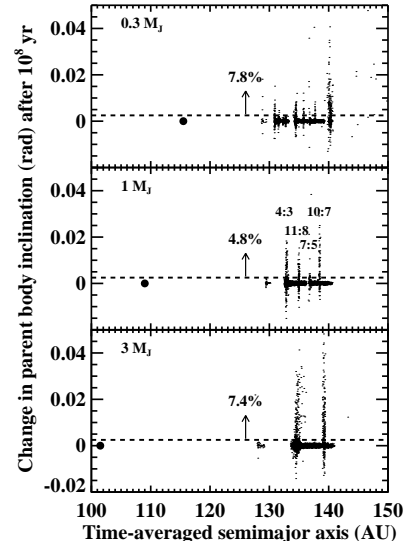


FIG. 7.— Changes in orbital inclinations of surviving parent bodies, evaluated after 10^8 yr. Solid circles denotes the planet. Only small percentages of stable parent bodies have their inclinations increased by the planet by more than 2.5×10^{-3} rad (0.14 deg); these percentages are indicated in each panel. For comparison, the initial distribution of inclinations extends uniformly from 0 to 2.5×10^{-2} rad. Those few objects that have their inclinations amplified are localized to mean-motion resonances, labelled only for the middle panel.

same invariant sharpness with planet mass characterizing the surface density profiles of our parent bodies.

The answer instead is that the sharpness of the inner edge does not depend only on the velocity dispersion of particles located strictly at the chaotic zone boundary. Particles located at some radial distance from the boundary, further interior to the belt, also contribute to the sharpness. That is because sharpness is a relative quantity, measured relative to the maximum of τ_\perp , and this maximum does not occur exactly at the chaotic zone boundary. Sharpness is appropriately measured as a relative quantity, since the observations are limited in dynamic range: as Figure 3 of K05 indicates, only the maximum in surface brightness, and values greater than $\sim 10\%$ of the maximum, are measurable.

To illustrate our point, we plot in Figure 8 the surface densities of stable parent bodies for two mass models, $0.3 M_J$ and $10 M_J$. For the comparison with Q06 to be fair, we must analyze only the parent bodies, since the conclusions of Q06 regarding inner edge sharpness pertain to collisionless, radiation-free particles; in other words, the test particles of Q06 are our parent bodies. From Q06 we would expect that the $10 M_J$ model produces an inner edge that is $(10/0.3)^{3/7} = 4.5 \times$ more diffuse, but the bottom panel of Figure 8 shows that this is not the case; in fact, if anything, the $0.3 M_J$ profile appears more diffuse. In the top panel of Figure 8 we show the same two models except that we include only particles having the smallest stable semimajor axes: $a < 132$ AU for $M_{\text{pl}} = 0.3 M_J$ and $a < 136$ AU for $M_{\text{pl}} = 10 M_J$. These profiles, which more strictly sam-

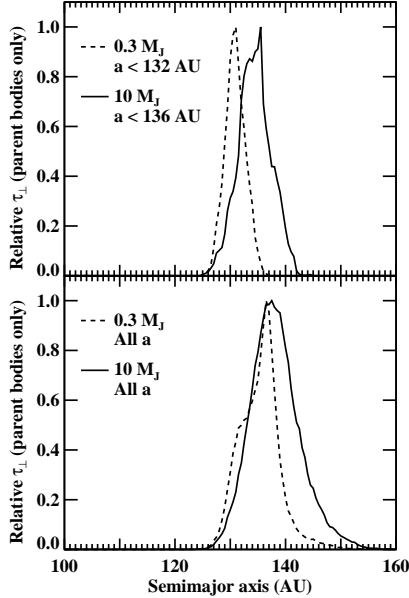


FIG. 8.— Reconciling our findings on the sharpness of the belt inner edge with those of Q06. *Top panel:* Surface density profiles of stable parent bodies for two mass models, $0.3M_J$ and $10M_J$, including only those bodies having the smallest semimajor axes as indicated (cf. Figure 5). Only parent bodies are considered to compare fairly with Q06, whose conclusions regarding inner edge sharpness pertain to collisionless, radiation-free test particles. In qualitative agreement with Q06, the $10M_J$ model yields a more diffuse inner edge, a consequence of that model’s larger velocity dispersion at the chaotic zone boundary (cf. Figure 6). *Bottom panel:* Surface density profiles of the same two models with no restriction on semimajor axes. Now the inner edges are of similar sharpness—in fact the $10M_J$ profile appears slightly sharper than the $0.3M_J$ model—indicating that sharpness is not uniquely related to edge velocity dispersion, contrary to the implicit assumption of Q06.

ple the chaotic zone boundary, are more consistent with Q06—the $0.3M_J$ profile is steeper than the $10M_J$ profile. We conclude that sharpness cannot be reliably computed without including contributions from particles that are located some distance from the edge. Sharpness cannot be calculated as if it were a local quantity specific to the minimum stable semimajor axis; the shape of the observed surface brightness profile reflects an amalgam of semimajor axes.

3.3.2. Variations in t_{col} and Gradual Release of Grains

According to our standard procedure, grain surface densities and optical depths from our β -simulations are extracted after an integration time of $t_{\text{col}} = 10^5$ yr, a value inspired from our order-of-magnitude estimate (9) of the collisional lifetime. In the top and middle panels of Figure 9, we demonstrate that our results are not sensitive to uncertainties in t_{col} . We present test results for $\beta = 0.2$ and $\beta = 0.4$ since those cases contribute most to τ_{\perp} for our assumed Dohnanyi size distribution. Varying t_{col} from 3×10^4 yr to 3×10^5 yr produces practically identical results for the surface density of grains. Only for the $\beta = 0.2$, $t_{\text{col}} = 3 \times 10^5$ yr run is there a slight ~ 1 AU shift of the surface density profile, a consequence of Poynting-Robertson drag. Such drag affects $\beta < 0.2$ grains even less. The highest β grains are also

relatively immune from pericenter decay—see the middle panel of Figure 9 for the case $\beta = 0.4$ —because of the large eccentricities and semimajor axes induced by radiation pressure upon release (Wyatt & Whipple 1950, see also our equation 10).

We can also check whether our simple procedure of releasing grains at a single time is sound. In reality, the belt at any given moment will contain grains having a variety of ages, ranging from 0 (just released grains) to t_{col} (grains just about to be shattered to sizes small enough to be blown out by radiation pressure). We better simulate the gradual release of grains by adding together surface density profiles computed from grains released at multiple times. We divide the interval t_{col} into 10 release times, uniformly spaced by $\Delta t = t_{\text{col}}/10$, and generate separate integrations for each time. That is, for the i^{th} release time, we integrate the stable parent bodies (generated from Step 1) forward with $\beta = 0$ for $i\Delta t$, and then continue integrating the released dust grains with $\beta \neq 0$ for $(10 - i)\Delta t$. The resulting superposition of integrations, for $\beta = 0.2$ and $t_{\text{col}} = 10^5$ yr, is shown in the bottom panel of Figure 9; it is nearly indistinguishable from our standard result. We have checked that ring shape is independent of grain age t for $1/\Omega \ll t < t_{\text{col}}$, because t_{col} is too short a time for grains to evolve away from their birth orbits (say by PR drag), and $1/\Omega$ is the timescale for grains to phase mix.

The experiments described in all three panels of Figure 9 also show that our standard surface density and optical depth profiles do not reflect dust features that vary with the orbital phase of the planet. In varying t_{col} and superposing snapshots taken at different times, we are extracting surface densities corresponding to random orbital phases of the planet.

3.3.3. Resonant Particles as Another Class of Stable Parent Body

All our parent bodies are initialized with purely forced eccentric orbits, as calculated using the Laplace-Lagrange secular theory. Their orbits after 10^8 yr resemble their initial ones, with the addition of a small free component.

Here we try a different set of initial conditions: osculating $e = 0$. According to L-L, this corresponds to assigning particles free eccentricities equal in magnitude to their forced eccentricities (see, e.g., Murray & Dermott 2000). The top panel of Figure 10 documents the resultant time-averaged semimajor axes of stable parent bodies (those that survive for 10^8 yr), for the case $M_{\text{pl}} = 0.3M_J$. All other initial conditions apart from the test particles’ eccentricities are specified the same way as for our standard $0.3M_J$ model. Remarkably, comparing the top panels of Figures 10 and 5, we find the distributions of stable semimajor axes are nearly complementary. Instead of being cleared out of mean-motion resonances, stable parent bodies inhabit them exclusively when initial eccentricities equal zero.

The resonances—which include the 7:6, 6:5, 5:4, 9:7, and 4:3, and which are of eccentricity-type—protect the particles from close encounters with the planet. Qualitatively, the eccentricities and apsidal angles behave as L-L predicts: while e cycles from 0 through $\max(e) = 2e_{\text{forced}} \approx 0.22$ back to 0, $\tilde{\omega}$ regresses from $\pi/2$ to $-\pi/2$ (the evolution of $\tilde{\omega}$ is discontinuous since e passes

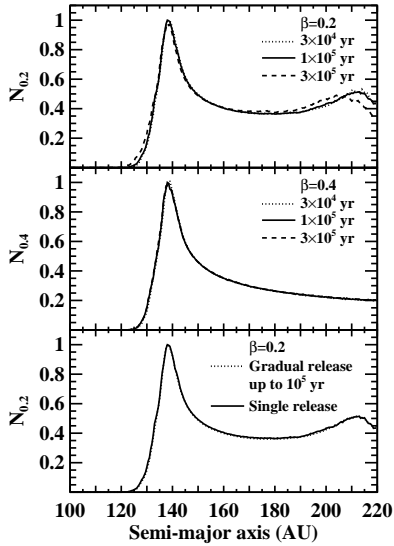


FIG. 9.— *Top panel:* Surface density profiles for $\beta = 0.2$ particles in our $1M_J$ model, as a function of t_{col} , whose value we only know to order of magnitude. Aside from a small inward shift caused by PR drag for $t_{\text{col}} = 3 \times 10^5$ yr, the profiles are not sensitive to our uncertainty in t_{col} . *Middle panel:* Same as top panel, except for $\beta = 0.4$. *Bottom panel:* Testing our simplifying assumption of a single release time for dust grains. Allowing grains to be released at ten uniformly spaced times between $t = 0$ and $t = 10^5$ yr produces no discernible difference from our standard model, which assumes a single release time of $t = 0$.

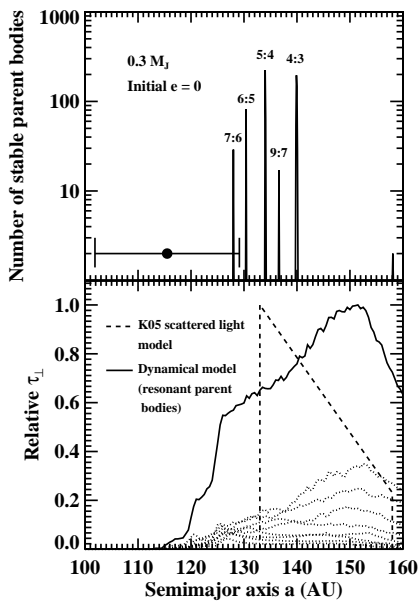


FIG. 10.— Experimenting with initially zero eccentricities for parent bodies, for the case $M_{\text{pl}} = 0.3M_J$. *Top panel:* Histogram of semimajor axes of parent bodies that survive for 10^8 yr, time-averaged over 10^5 yr. In stark contrast to our standard model (Figure 5), survivors only inhabit mean-motion resonances, which afford them protection from the close planetary encounters that would otherwise result from the large eccentricities that develop secularly. *Bottom panel:* Optical depth profile of dust generated by resonant parent bodies. It is far too broad to agree with the K05 model. We conclude that while resonant parent bodies can exist in principle, their population in reality must be small compared to that of parent bodies on nearly purely secularly forced orbits.

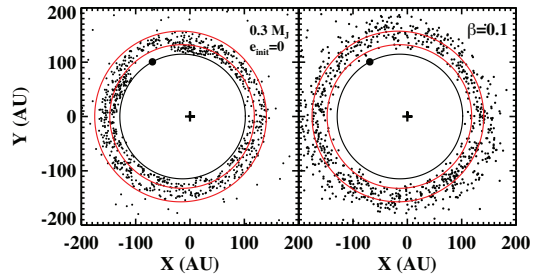


FIG. 11.— Same as Figure 1, except for resonant parent bodies. The left panel shows how resonant parent bodies avoid close encounters with the planet. The entire pattern corotates with the planet. Dust grains released from these resonant parent bodies have large eccentricities and yield an optical depth profile too broad to match that of K05; see Figure 10.

through 0). The large maximum eccentricities, which result because the free eccentricities are of the same magnitude as the forced eccentricities, put particles in danger of close planetary encounters, especially when $e = \max(e)$ and $\tilde{\omega} = 0$. Under these conditions, for a semimajor axis of, say, $a = 128$ AU, the particle's pericenter encroaches within ~ 2 AU $\approx 0.5R_H$ of the planet's pericenter.

However, thanks to resonance, conjunctions occur only at special orbital phases and close encounters do not occur. For the circumstances just described, during the phase that the particle attains maximum eccentricity, we have observed in our numerical integrations that conjunctions never occur at periastron. Because of the 7:6 resonance, they occur instead 180° degrees away, at apoapse, when the bodies are well separated by about 27 AU. Figure 11 provides a snapshot of stable resonant parent bodies, showing how they avoid approaching the planet.

Can such resonant parent bodies be present in Fomalhaut's belt? Not in significant numbers compared to the non-resonant population. The resonant bodies develop more eccentric orbits, and consequently the dust they produce is more spatially extended. From the bottom panel of Figure 10 (see also the right-hand panel of Figure 11), it is clear that the optical depth profile of dust released from resonant parent bodies is far too broad to match that of K05. (Our procedure of calculating optical depths by smoothing particles over their orbits is not correct for resonant objects, since the smoothing ignores their special orbital phase relationships with the planet. However the error accrued is small, since τ_{\perp} is dominated by dust particles having $\beta \gtrsim 0.1$. Such dust particles, upon release, have their semimajor axes increased by $\gtrsim 10\%$ by radiation pressure, and are thus removed from the resonances inhabited by their parents.)

In §4.3 we discuss how the parent bodies might have come to occupy nearly purely secularly forced orbits and to avoid the resonant orbits.

4. SUMMARY AND DISCUSSION

We review our main results in §4.1; sketch the effects of other planets apart from Fom b in §4.2; and discuss possible origins of Fom b and the belt in §4.3.

4.1. Summary

Fomalhaut b is the first extrasolar planet candidate to be directly imaged at visible wavelengths and to have its orbital motion around its host star measured. The Fo-

malhaut system also presents the first example of planet-disk interaction at a young age. Surprises have been immediate: Fomalhaut b has an unusually large orbital radius of more than 110 AU (cf. Lafrenière et al. 2008), and a visual ($0.45\text{--}0.7\ \mu\text{m}$) luminosity that is not only 1–2 orders of magnitude greater than atmospheric models anticipated, but also time variable. Nevertheless, a chain of arguments based on comparing the observed photometry with model exoplanet atmospheres leads Kalas et al. (2008, K08) to infer that the mass of Fomalhaut b must be less than about $3M_J$.

The Fomalhaut system is all the more remarkable for offering a means independent of model spectra to get at Fom b’s mass: the star is encircled by a belt of dust whose geometry is sensitive to the mass and orbit of Fom b. At a system age of ~ 200 Myr, detritus from the formation of the Fomalhaut planetary system still remains, and is gravitationally sculpted by Fom b. The observed intrinsic ellipticity of the ring almost certainly owes its origin to secular forcing by Fom b, which itself resides on a similarly eccentric orbit in this interpretation (Wyatt et al. 1999; Quillen 2006). Another feature of the belt likely influenced by Fom b is its inner edge. The observed sharpness with which the belt truncates reflects the sharp divide between stability and chaos at the boundary of the planet’s chaotic zone, inside of which first-order mean-motion resonances overlap and particle orbits are short-lived (Wisdom 1980; Quillen 2006). Particles inside the zone quickly evolve onto planet-crossing orbits and thereafter are perturbed onto escape trajectories.¹¹ Identifying the belt inner edge with the chaotic zone boundary relates the distance between the planet and the belt edge to the planet-star mass ratio.

Based on these and other theoretical ideas, we have built a realistic dynamical model of the Fomalhaut planet-belt system. Our goal is to calculate the spatial distribution of dust generated from the collisional comminution of larger parent bodies, and to compare our dust maps with the HST scattered light observations. The model begins by using numerical integrations to establish an annulus of parent bodies—a.k.a., the “birth ring” (Strubbe & Chiang 2006)—that is stable for 100 Myr against perturbations by Fom b. Dust particles are released from these dynamically stable parents, and their trajectories followed, taking additional account of stellar radiation forces, for a dust collisional lifetime of $t_{\text{col}} = 0.1$ Myr. The orbits of dust particles at the end of a t_{col} -long integration are assumed to represent well those of actual dust particles, which in reality have a range of ages extending up to $\sim t_{\text{col}}$. We have subjected this assumption to a few tests and found it to hold. Final dust particle orbits, computed for a range of radiation β ’s (force ratio between stellar radiation pressure and stellar gravity), are converted into orbit-averaged maps of relative surface density (number of grains per unit face-on area of the belt). A Dohnanyi (1969) grain size distribution, appropriate for a quasi-steady collisional cascade, is assumed to hold in the birth ring, where the dust surface density is highest and collision rate is greatest. This assumption determines how we weight and add the sur-

face density maps to produce a map of (relative) vertical optical depth. That optical depth map—or rather its azimuthally averaged version, the variation of optical depth with semimajor axis—is compared with the optical depth profile of the Kalas et al. (2005) scattered light model, which itself represents an idealized and approximate fit to the HST images.

A conservative result of our dynamical model is that $M_{\text{pl}} < 3M_J$. This conclusion, that Fom b must be of planetary mass, is entirely independent of Fom b’s photometry—and its uncertain interpretation. Our result stems from two simple and robust trends, neither of which involve inner edge sharpness, in contrast to Q06. First, as M_{pl} increases, dust particles are increasingly perturbed by the planet onto more eccentric orbits, rendering the dynamical profiles too broad compared to the scattered light profile. A mass of $10M_J$ yields a belt that is about twice as bright between 150 and 160 AU as the observations allow, while lower masses $M_{\text{pl}} < 3M_J$ give optical depth profiles that we feel agree adequately well with the Kalas et al. (2005) scattered light model. Second, given the observed location of the inner edge of the belt, larger mass planets have necessarily smaller orbits located farther interior to the belt, and smaller orbits may be incompatible with the observed stellocentric distance of Fom b. A mass of $10M_J$ requires an orbit whose apocentric distance is 107 AU, falling well short of our estimated de-projected distance for Fom b of 119 AU. By contrast, for $M_{\text{pl}} \leq 1M_J$, the model apocentric distances are ≥ 122 AU. While $3M_J$ yields an orbit whose apocenter lies at 115 AU and is nominally incompatible, uncertainties in the observed de-projected distance, probably amounting to a few AU, preclude us from ruling out this mass. Thus, erring on the safe side, we conclude that $M_{\text{pl}} < 3M_J$. Corresponding to these masses are orbital semimajor axes $a_{\text{pl}} > 101.5$ AU and eccentricities $e_{\text{pl}} \approx 0.11\text{--}0.13$.

It is heartening to see that our preferred mass range of $M_{\text{pl}} < 3M_J$ supports that inferred from the spectral models. And looking excitedly towards the future, we can expect to pinpoint the mass more precisely by combining our $M_{\text{pl}}(a_{\text{pl}})$ relation (see Table 1 and equation 16) with Fom b’s orbital semimajor axis once that is determined from multi-epoch astrometry.

For a taste of what might come, here is a bolder, less conservative analysis based on the limited data in hand. Though the planet’s orbit cannot be de-projected uniquely because its position has only been recorded twice, the same is not true for the belt. The brightest portions of the belt can be fitted to an apparent ellipse on the sky, and that apparent ellipse can be uniquely de-projected (K05; Smart & Green 1977). Then we can proceed by assuming Fom b’s apparent orbit on the sky is merely an isotropically scaled, miniature version of the belt’s apparent ellipse, making sure that this scaled ellipse intersects the two recorded positions of Fom b. Finally this scaled ellipse can be de-projected using the same de-projection solution derived from the belt. Such a procedure yields an intrinsic semimajor axis for Fom b’s orbit of 114.5 AU and—by extension using our equation (16)—a mass of $0.3\text{--}0.4M_J$, where the range reflects the 1 AU uncertainty in a_{inner} (§3.1.4). But this analysis is not complete, because the corresponding intrinsic eccentricity of the scaled ellipse (0.11) is about 10% too

¹¹ We estimate that planet crossing takes $\sim 10^5(10^{-3}/\mu)^{4/7}$ yr and ejection takes $\sim 10^7(10^{-3}/\mu)^2$ yr, for particles halfway between the planet and the edge of the chaotic zone.

small compared to what our dynamical models require for the planet (see Table 1). If the planet were located at apastron, increasing the eccentricity means that we should reduce the semimajor axis, so as to still fit the observed positions of Fom b. In fact, Fom b appears to have a true anomaly of about 109 deg, so the implied reduction in semimajor axis, and the consequent upward revision of planetary mass, is slight. A more detailed analysis is underway, but for now this preliminary and model-dependent interpretation of the limited astrometry is consistent with $a \approx 114$ AU and $M_{\text{pl}} \approx 0.4M_{\text{J}}$. The uncertainty on M_{pl} is difficult to gauge, but might span a factor of 2 in either direction.

Our findings agree in broad outline with those of Quillen (2006), whose prediction that the belt inner edge be located at the boundary of the planet’s chaotic zone is vindicated by the discovery of Fom b. We diverge from Quillen (2006) in how we determine Fom b’s mass. Among the improvements we make are: (1) we draw a clear distinction between unobservable parent bodies and observable dust grains, and rely on the latter when comparing with the HST scattered light observations; (2) we include the effect of stellar radiation pressure, significant for dust grains; (3) parent bodies are screened for dynamical stability over the age of the system; and (4) grain-grain collisions are recognized as destructive, and therefore the duration of each of our dust particle integrations is necessarily limited by the collision time. Our upper mass limit of $3M_{\text{J}}$ follows, in part, from comparing theoretical and observed optical depth profiles of dust, computed globally over all space, and from noting how steep those profiles are both inside and outside of the location of peak optical depth. By contrast, the upper mass limit derived by Quillen (2006), $\sim 0.2M_{\text{J}}$, follows from an analysis of the radiation-free dynamics of collisionless particles—essentially, the dynamics of parent bodies—local to the chaotic zone boundary, and from the assumption that the local velocity dispersion of such bodies determines the sharpness of the inner belt edge. Our calculation of the upper mass limit is preferred because the HST observations are of dust, not of parent bodies, and also because we have shown that edge sharpness is better computed using a global model such as ours.

Perhaps the biggest deficiency of our model lies in our crude treatment of grain collisions. In setting a dust particle’s initial position and velocity equal to that of its parent body, we ignore collisional dissipation and redirection of orbital kinetic energy. We also neglect the fact that grinding the largest parent bodies down to dust requires multiple collisions, and that radiation effects can start manifesting in the middle of the collisional cascade. For example, a particle for which radiation effects are significant, say which has $\beta = 0.4$, can be born from a parent body for which radiation effects were also significant, say which had $\beta = 0.2$. Still, our simple prescription of releasing dust grains having $\beta > 0$ from bodies having $\beta = 0$ is not without justification. Collisional energy dissipation should, on average, dampen free eccentricities but not forced eccentricities (see §4.3); thus the mean elliptical shape of the belt is expected to be preserved. Grain ejection velocities relative to the parent are distributed isotropically and should therefore not bias our results, though they will produce larger free eccentricities than our model predicts. Larger free eccentricities

will result in smoother optical depth profiles: a blurring of the belt (see §4.3 for further discussion of free eccentricities). Finally, radiation effects are predominantly felt over only the last decade in grain size above the blow-out size, i.e., only after the penultimate collision just prior to the final collision resulting in blow-out, for collisions that are strongly disruptive. The next generation of models should test these assertions, in addition to considering qualitatively different physics (e.g., Yarkovsky drag, and gas-particle interactions.¹²)

4.2. Other Planets In Addition to Fom b

While we have assumed throughout our study that Fom b is the only planet in the Fomalhaut system, multiple planets are also compatible with the observed belt eccentricity. In Laplace-Lagrange theory, the observed forced eccentricity vector of a belt particle equals the vector sum of n eccentricity vectors forced by n planets. Because the individual eccentricity vectors precess at frequencies that depend only on the fixed masses and semimajor axes of the planets (these are the fixed eigenfrequencies of the linear theory), and because belt particles having similar semimajor axes have similar vector decompositions, we expect the forced eccentricity vectors of belt members to remain similar to one another over time. Thus a narrow belt can maintain a global mean eccentricity in the presence of multiple planets, though that mean eccentricity will oscillate with time. All these considerations can be accommodated if necessary into our modelling procedure.

Nevertheless, given the observed proximity of Fom b to the belt, a case can be made that Fom b dominates the forced eccentricities of belt particles. A possible analogy would be Neptune and the Kuiper belt. Despite the existence of as many as four giant planets in our solar system, the forced inclination and eccentricity vectors of Kuiper belt objects are largely determined by the nearest planet, Neptune (see, e.g., Chiang & Choi 2008). If indeed Fom b dominates the belt’s secular dynamics, then we expect its orbit to be apsidally aligned with that of the belt. If future astrometry reveals a significant apsidal misalignment, then at least one other, as yet unseen planet would be implicated. In that case, because the belt’s forced eccentricity is a vector sum, Fom b’s eccentricity could either be lower or higher than the eccentricity we have calculated, depending on the apsidal orientation(s) of the other planetary orbit(s).

How would additional planets affect our determination of Fom b’s mass? Broadly speaking, more planets render more of orbital phase space chaotic. Therefore Fom b, if abetted by other planets, can have a smaller mass and still truncate the belt at its observed inner edge. The upper limit of $3M_{\text{J}}$ that we have calculated is, in this sense, a hard upper limit.

Intriguingly, over its three-year mission, the Hipparcos satellite observed Fomalhaut to have an “anomalous” proper acceleration of 6.6 milliarcsec/yr². Such a quasi-steady acceleration might be caused by a companion

¹² Fomalhaut’s closest analogue may be AU Mic, insofar as both have birth ring morphologies and similar optical depths (Strubbe & Chiang 2006). Gas has not been detected in AU Mic (Brandeker et al., 2008 Spitzer Science Conference Poster #81). The β Pic debris disk, containing plenty of metallic gas (Brandeker et al. 2004), remains an anomaly.

whose orbital period is longer than ~ 3 years, or equivalently whose stellocentric distance $r \gtrsim 3$ AU. Equating the measured acceleration with $(GM/r^2)/d$, where M is the perturbing mass and $d = 7.7$ pc is the distance to Fomalhaut, we see that Fomalhaut might also be harboring a $\sim 30M_J$ brown dwarf at a distance $r \sim 5$ AU. (Larger r implies larger M and such solutions are probably ruled out by observation. Clearly Fom b cannot be responsible for the Hipparcos acceleration.) Compared against the influence of Fom b as we have computed it in this paper, such a brown dwarf would contribute less than 10% to the forced eccentricity of a belt particle, if the brown dwarf's eccentricity $\lesssim 0.2$.

4.3. Parent Body and Planet Origins

Though the direct detection of parent bodies is beyond the reach of current observations, our study has provided some evidence that they reside mostly on nearly purely secularly forced orbits with small free eccentricities. In principle, they do not have to; we found by experimentation in §3.3.3 that large free eccentricities are also compatible with long-term stability if the particles are protected by mean-motion resonances.

How did the parent bodies choose one class of stable orbit over the other? The answer, as suggested also by Quillen & Faber (2006), likely involves collisional dissipation. Collisions dissipate random orbital motions and compel planetesimals to conform towards closed, non-intersecting orbits viewed in the frame rotating with the perturbation potential (e.g., Paczynski 1977; Goldreich & Tremaine 1982, section 5.4). If that perturbation potential arises from Fom b, the special closed orbits include the secularly forced orbits that we have been highlighting throughout our study, but they do not include the resonant orbits that emerged from our experiment. Collisional dissipation and relaxation onto closed orbits occur across the entire collisional cascade, up to the largest parent bodies (which by definition collide once over the system age).

We do not expect the destructive nature of collisions to qualitatively alter this picture, since what is important here is the dissipation of random kinetic energy, and that occurs whether or not collisions are destructive. Post-

collision fragments will have free eccentricities that are small compared to forced eccentricities, insofar as post-collision fragment velocities (measured relative to the center of mass) are small compared to $e_{\text{forced}}\Omega_R R \sim 400$ m/s. At least in the collisional genesis of the Eunomia and Koronis asteroid families in our solar system's main belt, ejection velocities of the largest post-collision remnants range from 4 to 90 m/s (Michel et al. 2001).

It is also possible that relaxation occurred while the parent bodies were forming, when collisions were gentler and agglomerative. The process of relaxation onto forced orbits can be explored using fast numerical simulation techniques for inelastically colliding, indestructible particles (Lithwick & Chiang 2007); in fact, we have started to run such simulations and clearly observe relaxation.

What are the origins of Fom b and the belt? It seems likely that the belt is what remains of the original disk material that went into building Fom b. If we take the minimum parent body mass of $3M_{\oplus}$ (estimated in §2.6) and augment it by a factor of 10^2 to bring it to cosmic composition, then the minimum primordial mass for the belt is $\sim 1M_J$. This is comparable to our estimated upper mass limit for Fom b. A working hypothesis is that Fom b accreted *in situ* from a primordial disk of gas and dust; that the hydrogen gas of the original disk has either accreted into planets or photoevaporated; and that today the remaining solids in the belt are grinding down to dust, the in-plane velocity dispersion of parent bodies excited so strongly by Fom b that collisions are destructive rather than agglomerative. The last tenet is supported by our Figure 6, which shows free eccentricity dispersions that imply relative parent body velocities upwards of ~ 100 m/s (see also our §2.3).

This work was supported by NSF grant AST-0507805. E.K. acknowledges support from a Berkeley Fellowship. We thank Mike Fitzgerald, Yoram Lithwick, Christian Marois, Norm Murray, Karl Stapelfeldt, and Mark Wyatt for discussions. An anonymous referee rapidly provided a thoughtful report, at the behest of ApJ Scientific Editor Fred Rasio, for which we are grateful.

REFERENCES

- Backman, D. E. & Paresce, F. 1993, in *Protostars and Planets III*, ed. E. H. Levy & J. I. Lunine, 1253–1304
- Barrado y Navascués, D. 1998, *A&A*, 339, 831
- Barrado y Navascués, D., Stauffer, J. R., Hartmann, L., & Balachandran, S. C. 1997, *ApJ*, 475, 313
- Brandeker, A., Liseau, R., Olofsson, G., & Fridlund, M. 2004, *A&A*, 413, 681
- Burns, J. A., Lamy, P. L., & Soter, S. 1979, *Icarus*, 40, 1
- Burrows, A., Sudarsky, D., & Lunine, J. I. 2003, *ApJ*, 596, 587
- Canup, R. M. & Ward, W. R. 2002, *AJ*, 124, 3404
- Chiang, E. & Choi, H. 2008, *AJ*, 136, 350
- Dohnanyi, J. W. 1969, *J. Geophys. Res.*, 74, 2531
- Duncan, M., Quinn, T., & Tremaine, S. 1989, *Icarus*, 82, 402
- Fortney, J. J., Marley, M. S., Saumon, D., & Lodders, K. 2008, *ArXiv e-prints*, 805
- Goldreich, P. & Tremaine, S. 1982, *ARA&A*, 20, 249
- Holland, W. S., Greaves, J. S., Zuckerman, B., Webb, R. A., McCarthy, C., Coulson, I. M., Walther, D. M., Dent, W. R. F., Gear, W. K., & Robson, I. 1998, *Nature*, 392, 788
- Hubickyj, O., Bodenheimer, P., & Lissauer, J. J. 2005, *Icarus*, 179, 415
- Kalas, P., Graham, J. R., & Clampin, M. 2005, *Nature*, 435, 1067
- Lafrenière, D., Jayawardhana, R., & van Kerkwijk, M. H. 2008, *ArXiv e-prints*
- Lithwick, Y. & Chiang, E. 2007, *ApJ*, 656, 524
- Marois, C., Macintosh, B., & Barman, T. 2007, *ApJ*, 654, L151
- Michel, P., Benz, W., Tanga, P., & Richardson, D. C. 2001, *Science*, 294, 1696
- Mosqueira, I. & Estrada, P. R. 2003, *Icarus*, 163, 198
- Murray, C. D. & Dermott, S. F. 2000, *Solar System Dynamics* (Cambridge: Cambridge University Press)
- Paczynski, B. 1977, *ApJ*, 216, 822
- Quillen, A. C. 2006, *MNRAS*, 372, L14
- . 2007, *MNRAS*, 377, 1287
- Quillen, A. C. & Faber, P. 2006, *MNRAS*, 373, 1245
- Smart, W. M. & Green, R. M. 1977, *Textbook on Spherical Astronomy* (Textbook on Spherical Astronomy, by William Marshall Smart and Edited by Robin Michael Green, pp. 446. ISBN 0521291801. Cambridge, UK: Cambridge University Press, July 1977.)
- Song, I., Caillault, J.-P., Barrado y Navascués, D., & Stauffer, J. R. 2001, *ApJ*, 546, 352
- Strubbe, L. E. & Chiang, E. I. 2006, *ApJ*, 648, 652
- Thébaud, P. & Wu, Y. 2008, *A&A*, 481, 713

TABLE 1
POSSIBLE PROPERTIES OF FOM B AND NUMBERS OF SURVIVING BELT PARTICLES

M_{pl} (M_{J})	a_{pl} (AU)	e_{pl}	N_{tp} ($t = 0$)	N_{tp} ($t = 10^8$ yr)	N_{tp} (0) ^a	N_{tp} (0.00625)	N_{tp} (0.0125)	N_{tp} (0.025)	N_{tp} (0.05)	N_{tp} (0.1)	N_{tp} (0.2)	N_{tp} (0.4)
0.1 ^b	120	0.115	10 ⁴	5798	5798	5796	5798	5798	5798	5798	5798	5727
0.3	115.5	0.118	10 ⁴	4471	4471	4467	4471	4471	4471	4471	4470	4421
1	109	0.123	10 ⁴	4191	4191	4191	4191	4191	4191	4191	4191	4187
3	101.5	0.130	10 ⁴	4466	4466	4456	4454	4465	4465	4466	4466	4456
10 ^c	94	0.138	10 ⁴	1548	1548	1546	1539	1433	1033	1460	1528	1548

^aThe pure number in parentheses for this column and subsequent columns equals β . All β -simulations tabulated here are integrated for $t_{\text{col}} = 10^5$ yr, following the 10^8 -yr-long parent body integration.

^bFor our 0.1 M_{J} run, initial parent body semimajor axes extend from 125 AU to 140 AU.

^cThe 10 M_{J} run is not favored since it produces a vertical optical depth profile that does not match that of the K05 scattered light model.

Wisdom, J. 1980, AJ, 85, 1122

—. 1982, AJ, 87, 577

—. 1983, Icarus, 56, 51

—. 1985, Icarus, 63, 272

Wisdom, J. & Holman, M. 1991, AJ, 102, 1528

Wyatt, M. C. 2005, A&A, 433, 1007

Wyatt, M. C., Dermott, S. F., Telesco, C. M., Fisher, R. S., Grogan,

K., Holmes, E. K., & Piña, R. K. 1999, ApJ, 527, 918

Wyatt, S. P. & Whipple, F. L. 1950, ApJ, 111, 134